Title

Functional Imaging of Cerebral Oxygenation with Intrinsic Optical Contrast and Phosphorescent Probes

Authors

Devor, Anna
Sakadžić, Sava
Yaseen, Mohammad A
et al.

Publication Date

2014

DOI

10.1007/978-1-62703-785-3_14

Peer reviewed

Chapter 14

Functional Imaging of Cerebral Oxygenation with Intrinsic Optical Contrast and Phosphorescent Probes

Anna Devor, Sava Sakadžić, Mohammad A. Yaseen, Emmanuel Roussakis, Peifang Tian, Hamutal Slovin, Ivo Vanzetta, Ivan Teng, Payam A. Saisan, Louise E. Sinks, Anders M. Dale, Sergei A. Vinogradov, and David A. Boas

Abstract

Microscopic in vivo measurements of cerebral oxygenation are of key importance for understanding normal cerebral energy metabolism and its dysregulation in a wide range of clinical conditions. Relevant cerebral pathologies include compromised blood perfusion following stroke and a decrease in efficiency of single-cell respiratory processes that occurs in neurodegenerative diseases such as Alzheimer's and Parkinson's disease. In this chapter we review a number of quantitative optical approaches to measuring oxygenation of blood and cerebral tissue. These methods can be applied to map the hemodynamic response and study neurovascular and neurometabolic coupling, and can provide microscopic imaging of biomarkers in animal models of human disease, which would be useful for screening potential therapeutic approaches.

Key words O_2 sensing, Phosphorescence quenching, Intrinsic optical signals, Energy metabolism, In vivo imaging, Hemoglobin, Two-photon microscopy, CCD

1 Introduction

Cerebral oxygenation and O_2 metabolism are key parameters defining healthy brain function. Until recently, though, our knowledge of the microscopic dynamics of cerebral oxygenation has been limited by a lack of methods with the spatial and temporal resolution needed to follow oxygenation changes induced by varying neuronal activity. Most of what we know about the behavior of cerebral oxygenation during the hemodynamic response comes from measurements of light absorption by hemoglobin in the blood. This method, commonly referred to as "optical imaging of intrinsic signals (OIS)", is based on differential absorption spectra of oxy- and deoxy-hemoglobin (HbO and Hb) in the visible range and does not require

Bruno Weber and Fritjof Helmchen (eds.), *Optical Imaging of Neocortical Dynamics*, Neuromethods, vol. 85,
DOI 10.1007/978-1-62703-785-3_14,

loading of extrinsic O_2-sensitive probes. Following the original demonstration [1], the intrinsic imaging method was widely used for investigation of neuro-hemodynamic coupling [2–11] and mapping of cortical neuronal responses [12–15] (Box 1).

The hemoglobin molecule is composed of four monomers, each containing an O_2-binding heme group. Hemoglobin tetramer

Box 1 Optical Imaging of Intrinsic Signals—A Historical Perspective

One hundred and twenty years ago, Roy and Sherrington [16] argued that neuronal activation causes the local vasculature to respond. While unequivocal confirmation of this claim had to wait nearly a century, until radioactive methods became available [17–20], large reflectance changes of brain tissue during localized seizure activity could be visualized already in the late 1930s [21]. A few decades later advances made it possible to detect and analyze the much smaller optical signals during activity of the normal cortex. These were accounted for by activity-associated changes in cerebral blood flow (CBF) and volume (CBV) [18, 22]; in addition, Chance [23] and Jöbsis [22] observed that neuronal activity is often accompanied by oximetric signals that can be detected optically by monitoring the absorption (and/or fluorescence) of hemoglobin and other intrinsic chromophores.

In the late 1980s, Grinvald et al. [1] showed that the small light absorption changes induced by these activity-evoked hemodynamic responses can be used to explore cortical functional architecture in vivo, by using a CCD camera to image the cortex upon illumination at specific wavelengths during the presentation of sensory stimuli. The resulting cortical images can then be used to produce functional maps at the spatial resolution of a few tens of microns, more than enough to image the columnar structure of the mammalian neocortex.

Since then, the interpretation of intrinsic signals in terms of neuronal activity—and thus their utility for functional brain mapping—has been tightly linked to our understanding of the mechanisms underlying neurovascular coupling. In fact, such knowledge is necessary to distinguish between optical signals resulting from changes in the activity of local neuronal populations and those resulting from the vascular effects of remote neuronal events (e.g., venous drain). To address this issue, Frostig et al. [4] imaged the sensory-evoked optical responses in the cortex at several wavelengths and tried to decompose them spectroscopically into CBV and O_2 saturation. A few years later, Malonek and Grinvald [6] used a continuous wavelength spectroscopic approach, optical imaging spectroscopy, to investigate the hemodynamic response in further detail. Both studies concluded that some hemodynamic events colocalize better with neuronal activity than others. In particular, an early increase in deoxy-hemoglobin concentration (Hb)—the so-called initial dip—was detected, and interpreted as resulting from local O_2 consumption induced by neuronal activity while the vasculature is still at rest. Thus, the initial dip is expected to colocalize more accurately with neuronal activity than the subsequent hemodynamic events, i.e., increased CBV and CBF, which are mediated by the complex spatiotemporal transfer function of the active vascular response [11, 24]. Which hemodynamic response component is best for functional mapping and how to optimally choose the imaging parameters (wavelength, timing of data acquisition, etc.) are therefore still the object of some debate [8, 25–31].

Whatever its conclusion, de facto, imaging the activity of visual stimuli in early visual cortex using oximetric wavelengths (600–630 nm, emphasizing changes in [Hb] over those in [HbO]) has allowed investigators to obtain high-quality single-condition functional maps, i.e., maps obtained by comparing stimulated conditions to rest. This has not been possible using isosbestic wavelengths, where Hb and HbO absorb with equal strength and which thus emphasize changes in CBV. At those wavelengths, differential approaches (the comparison of several stimulated conditions one to another) are needed to visualize functional architecture at the columnar level [4, 24], at least upon stimulation with large visual stimuli. Interestingly, in other cortices such as auditory [32–34] and rat somatosensory cortex [26], CBV-based optical signals have turned out to warrant at least as good mapping as oximetric ones. Moreover, in primate visual cortex [30] it has been shown that, upon stimulation with small

(continued)

Box 1 (continued)

retinotopic stimuli, the resolution of CBV-dominated signals is as precise as that obtained using oximetric ones.

Taken together, these accumulating results indicate that the optimal choice of the signal to be used for functional mapping might depend on the relation between the topology of the local vascular network and that of the functional architecture to be mapped, that is, on the specific cortical area. However, kind and duration of the stimulus, as well as the signals' etiology, must also be taken into account (e.g., the CBV response appears to have an early capillary component and a delayed macrovascular one), in rodents [27, 35, 36] and primates [30]. Finally, it has been shown that, under some circumstances, imaging at long wavelengths (>700 nm) is advantageous in spite of the small signal sizes, because it reduces the contribution of surface vasculature [37]. Yet, the precise composition of the optical signal at those wavelengths remains to be determined [38].

Irrespective of the above issues, detailed maps of the cortical functional architecture have been obtained in a large variety of preparations—from rodent through cat and ferret up to the primate—in several cortical areas, including both sensory (visual, auditory, somatosensory) and motor. In early visual cortex, intrinsic imaging of functional domains was first reported by Grinvald et al. [1] and later on by many others [39–42]. These studies have laid the groundwork for optical imaging of higher visual areas such as MT [43], V4 [44], and inferotemporal cortex [45]. Fine functional organization of auditory cortex revealed by Fourier optical imaging was reported by Kalatsky et al. [46], after earlier work by Frostig and co-workers [47] and other groups. In the somatosensory cortex, the visualization of whisker barrels in the rat has been a standard protocol for nearly 20 years now [48]. Moreover, the representation of functional domains for digits [49–51] and recently the representation of mechanical nociceptive stimuli within SI have been reported [52].

The elimination of anesthesia has been another critical step. High-resolution optical imaging in alert monkeys was first reported by Grinvald et al. [53], and later in trained monkeys by Roe's group [54]. However, the challenge of long-term imaging in the awake behaving primate could be met only with the development of an artificial, transparent dura substitute [14, 55, 56]. This has allowed investigation not only of the functional architecture but also of its stability over time [14], as well as its behavioral correlation with neurophysiology [15]. Optical imaging has also enabled long-term developmental studies such as imaging the development of orientation preference maps [57, 58] and the layout of functional domains in strabismic animals [59, 60].

Due to its high resolution and non-invasiveness, optical imaging of intrinsic signals has also been used to explore pathological situations, such as the exploration of epilepsy, in animal models as well as in humans [61, 62] and in intraoperative imaging in humans [63, 64], with the goal of finely localizing the site of specific cortical functions.

exists in equilibrium between two states (T and R), characterized by different affinity to O_2. The O_2 binding to hemoglobin is allosterically regulated in the sense that the binding itself shifts the equilibrium towards the higher affinity R state (for review see [65]). Conformationally the T and R states are different, but their optical absorption spectra are very similar. In contrast, binding of O_2 to a heme group induces significant spectroscopic changes. Therefore, each monomer in the hemoglobin molecule, whether it exists in the T or in the R state, can be considered an independent chromophoric unit.

During an increase in neuronal activity, the associated increase in flow and volume of blood results in a decrease of O_2 extraction fraction (from blood to tissue) producing a decrease in deoxyhemoglobin concentration ([Hb]) and an increase in oxyhemoglobin concentration ([HbO]). This effect can be detected,

for example, by a decrease in light absorption at 580 nm and the corresponding changes in the absorption-based image (for a recent example from rat somatosensory cortex see [66]). Thus, mapping of neuronal activity can be achieved using a simple epi-illumination/reflectance setup and a CCD camera for detection. Multi-wavelength illumination [6] can be used to extend this method to quantify HbO and Hb changes (as % change from the baseline) [38, 67, 68]. Such absorption-based measurements are linearly related to the fraction of O_2 bound to hemoglobin, while their relationship to the blood pO_2 (dissolved O_2) is defined by the non-linear hemoglobin O_2 binding curve.

An alternative approach to quantifying intravascular O_2 changes in the brain is based on introducing extrinsic phosphorescent probes into the blood stream [25, 69–71,] and measuring phosphorescence lifetime. The method—namely the use of phosphorescence quenching to quantify O_2 tension—was originally developed by Wilson and colleagues [72, 73] and relies on the fact that molecular oxygen (O_2)—a triplet molecule in the ground state—is able to quench emission from excited triplet states of other molecules, such as phosphorescent metalloporphyrin-based probes. Thus, while the intrinsic imaging method measures hemoglobin oxygenation, the phosphorescence quenching technique detects O_2 by measuring kinetics of quenching. Therefore, it can be applied for both intravascular and tissue measurements, given an adequate strategy for delivery of the probe. The phosphorescence lifetime of a probe depends on the partial pressure of O_2 (pO_2) in the immediate vicinity of the probe, providing a spatially localized measurement. O_2 is the only effective dynamic quencher of phosphorescence present in biological systems in sufficient concentration, so measurements of phosphorescence report O_2 levels with high specificity. Importantly, the decay lifetime (rather than the phosphorescence intensity) is measured, which makes the technique insensitive to local variations in the probe concentration and, very importantly, to changes in tissue optical properties. As such, lifetime measurements are insensitive to the absorption and scattering changes associated with the hemodynamic response in vivo, as long as a sufficient number of photons reach the detector for the accurate fitting of the phosphorescent decay. A brief discussion of phosphorescent probes can be found in Box 2 below as well as in recent papers (see, for example, [74, 75]).

Imaging with intrinsic hemoglobin-based contrast or with phosphorescence in wide-field mode using a CCD camera has no true depth resolution: the signal at every pixel represents a weighted sum of the response through the whole depth of light penetration with the highest sensitivity to the cortical surface. This limitation might be acceptable for certain types of intravascular studies, in particular, studies of the "columnar" organization of circulation in cerebral cortex: the vertical orientation of diving arterioles and, more importantly, surfacing venules, transporting

Box 2 Phosphorescent O_2 Sensors

The ideal phosphorescent O_2 probe for in vivo applications consists of a phosphorescent chromophore of the maximal attainable brightness, encapsulated inside a protective jacket, the role of which is to regulate O_2 diffusion to the chromophore (and thereby constant k_q, Eq. 2) in order to maintain high O_2 sensitivity throughout the physiological range. Unrestricted O_2 access (too high k_q) leads to complete quenching of phosphorescence already at low O_2 concentrations, whereas overly restricted access (low k_q) results in a narrow dynamic range, i.e., the difference between the phosphorescence of the quenched and unquenched probes is too small. Similarly, too short triplet lifetimes result in low sensitivity because of low probability of collisions with O_2.

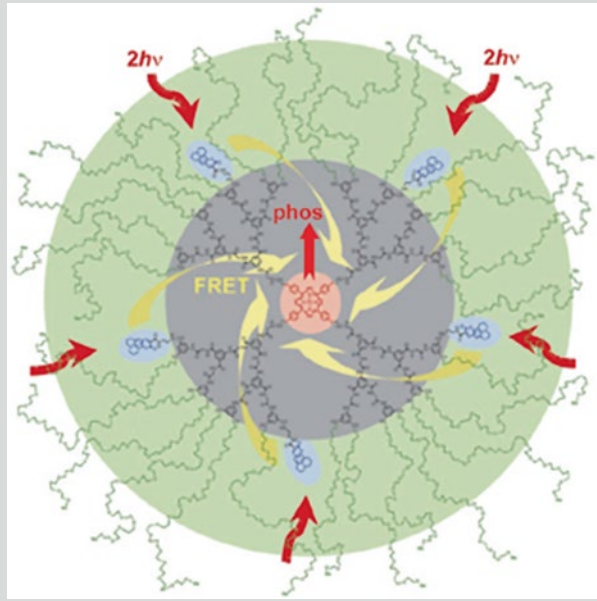

Fig. B1 Molecular structure of PtP-C343. PtP-C343 is a dendritic O_2 probe, in which phosphorescence of metalloporphyrins upon two-photon excitation is enhanced by intramolecular Förster resonance energy transfer (FRET) from two-photon coumarin-343 antennae chromophores (*blue*). The O_2 sensitivity of the probes is regulated by dendritic encapsulation of the core metalloporphyrin (*gray*), while peripheral polyethyleneglycol residue groups on the dendrimer isolate the probes from contact with biological macromolecules in the environment (*green*).

Only a few chromophores exhibit bright phosphorescence in solutions at ambient temperatures. Based on the optical spectra, emission quantum yields, and triplet lifetimes, porphyrins of Pt and Pd are by far the best suited for O_2 measurements in the physiological pO_2 range. The original probes were based on simple derivatives of Pd porphyrins [73, 76]. Such porphyrins are relatively hydrophobic and need to be prebound to serum albumin (usually bovine albumin) to improve their solubility and prevent aggregation in aqueous media. As a result, exogenous protein becomes a part of the injected material, which may lead to unwanted immunogenic reactions and possible toxicity.

Introduction of dendritic polyglutamic porphyrins [77, 78], known as Oxyphors R2 and G2, alleviated the necessity of pre-binding probes to albumin, thanks to polyglutamic branches which render the compounds highly water-soluble. Nevertheless, Oxyphors R2 and G2 still require binding to endogenous albumin, because only albumin complexes of these probes are suitable for measurements in the physiological O_2 range [79]. As a result, O_2 measurements with R2 and G2 can be performed only in albumin-rich environments (e.g., blood plasma). Even in the blood, though, incomplete binding, easily

(continued)

Box 2 (continued)

encountered at high probe concentrations (above ~10^{-5} M), can lead to heterogeneous decays and compromise measurement accuracy.

Keeping the calibration constants of probes unaltered in biological systems is a significant challenge, but also a stringent requirement for quantitative imaging. Indeed, it is not sufficient to have a luminescent probe whose signal simply changes in response to O_2. It is important that both k_q and τ_0 (Eq. 2) remain exactly the same as they were determined during the calibration. These probes' parameters are defined by the probes' immediate environment; to insure their stability the probe molecule must remain in aqueous phase, forming no complexes with bio-macromolecules, cellular membranes, or other biological objects. These requirements have been fulfilled in the so-called fully protected third-generation probes [74, 80]. Pt or Pd porphyrins in these probes are encapsulated inside hydrophobic polyarylglycine (AG) dendrimers, whose exteriors are modified with hydrophilic polyethyleneglycol (PEG) residues. PEGylated jackets regulate the sensitivity and dynamic range of the measurement and insure the probes' high aqueous solubility and inertness with respect to the biological system. This general design is inherent in both one- and two-photon (vide infra) O_2 probes.

To enable two-photon phosphorescence lifetime microscopy (2PLM), special phosphorescent probes were recently developed with enhanced two-photon absorption cross sections. One such probe is PtP-C343 [81], which has been successfully utilized in vivo in brain imaging studies [82–84]. The functional elements of PtP-C343 are Pt tetraarylporphyrin (PtP), which acts as a phosphorescent core, and several C343 units, which play the role of the two-photon antenna (Fig. B1). Near-infrared energy (e.g., at 840 nm) is absorbed by the C343-antenna and within fractions of a nanosecond channeled to PtP via intramolecular FRET, where it is utilized to populate the emissive triplet excited state. The redox potentials of PtP and C343 and the distances between them within the probe molecule are optimized to minimize the unwanted triplet quenching by electron transfer [80, 81]. The C343-antenna enhances phosphorescence in PtP-C343 approximately 25-fold compared to that or a regular one-photon probe. Because of the effect of the dendritic layer and peripheral PEG groups, PtP-C343 is pH-insensitive in the physiological range and its signal is independent of interactions with proteins in the blood.

the deoxygenated blood along the imaging axis. Sensing tissue oxygenation, however, has a stronger requirement for the resolution in depth. Indeed, metabolic differences between cortical layers have been demonstrated with other methods, e.g., cytochrome oxidase staining and incorporation of 2-deoxyglucose [85–87]. In recognition of the importance of depth-resolved tissue pO_2 measurements, numerous studies have employed point polarographic O_2 sensors, also called "O_2 electrodes" [88]. While measurements with O_2 electrodes have provided invaluable insight into tissue O_2 dynamics in cerebral [89, 90] and cerebellar cortex [91], the point nature of the measurement, blind positioning, and invasiveness of the method—the need for repetitive penetrations throughout the cortical tissue for mapping the signal at different locations—put significant constraints on throughput and data interpretations. Indeed, O_2 electrode measurements have demonstrated a significant degree of unaccounted for variability between nearby locations, which could result from differences in the electrode position relative to the blood vessels and/or tissue damage associated with electrode insertion [92, 93]. O_2 electrodes have been successfully used to map oxygenation on the cortical surface [94–96], circumventing the uncertainty of blind positioning. Other methods of measuring tissue O_2 include binding of nitroimidazole-based

drugs [97] and electron paramagnetic resonance (EPR) oximetry [98, 99]. These methods differ in spatial and temporal resolution, but generally cannot be applied to real-time tissue O_2 microscopy.

Several new approaches to tissue oximetry have recently been disclosed. First, imaging modalities based on photo-acoustic effect (photo-acoustic tomography [PAT], photo-acoustic microscopy [PAM], optical resolution photo-acoustic microscopy [OR-PAM]) are capable of volumetric measurements of the Hb/HbO ratio [100] with an optical contrast and, except in the case of OR-PAM, ultrasound resolution. Due to the low scattering of sound waves, the imaging resolution of PAT is much higher than that of Diffuse Optical Tomography (DOT), e.g., sub-millimeter resolution at depths as high as 50 mm. However, direct comparisons of O_2 images obtained by the two methods have yet to be performed. Also, penetration depth of PAM is higher than that of current optical microscopy technologies (e.g., two-photon microscopy and optical coherence tomography). Second, a microscopic O_2 imaging method has been described by Warren and collaborators [101] who quantified the Hb/HbO ratio by measuring the excited state absorption of the two components using multiphoton absorption and excitation by shaped femtosecond infrared pulses. This technique is subject to the same depth limitations as all methods relying on ballistic photons and, like DOT, suffers from low sensitivity. A variant of luminescence quenching technique has recently been described by Ashkenazi et al. [102] who measured triplet kinetics using transient triplet–triplet absorption and acoustic detection. However, generation of adequate acoustic signals requires very high probe concentrations and/or near-saturation excitation regime in order to produce adequate amounts of the triplet state. Finally, a method is being developed, which is based on the dependence between the time-averaged fluorescence intensity of regular fluorescent dyes and population of dark triplet states of these dyes in O_2-dependent fashion [103, 104]. This approach also requires extremely high excitation intensities, unlikely to be sustainable by biological tissues.

Seeking to overcome the problem of spatial resolution in CCD-based wide-field imaging of pO_2 based on O_2-dependent phosphorescence quenching, some studies have attempted to combine the phosphorescent quenching method with two-photon excitation [71, 105]. Unfortunately, regular metalloporphyrin-based phosphorescent probes have very low two-photon absorption cross sections, and therefore require extremely high probe concentrations and high laser powers to observe adequate signals. Probes such as Oxyphor R2 [77, 79] and simple hydrophilic Pd porphyrins [73], which can operate only as complexes with albumin (vide infra), partially exist in unbound form at such high concentrations. As a result, the phosphorescence decays are characterized by complex lifetime distributions and cannot be interpreted quantitatively. To enable 2PLM of O_2, special two-photon-enhanced phosphorescent probes have recently been

designed [80, 81, 106]. Here, two-photon-"antenna" chromophores are included in the probe molecules for the purpose of capturing excitation energy and transmitting the excitation to phosphorescent cores via intramolecular Förster resonance energy transfer (FRET).

The other major obstacle precluding widespread use of two-photon excitation of phosphorescent probes is a temporal mismatch between high repetition rates of femtosecond Ti:sapphire lasers, typically used for multiphoton excitation (~80 MHz), and long triplet lifetimes of porphyrin-based probes (tens to hundreds of microseconds). To circumvent this problem, the excitation must be gated to allow for acquisition of the phosphorescence decay. Commercial systems suitable for simultaneous measurement/imaging of phosphorescent lifetimes during the gate off-time and fluorescent lifetimes during the gate on-time are just starting to appear (Becker & Hickl data acquisition boards SPC-830 and SPC-150, http://www.becker-hickl.de). However, it is possible to modify or build a 2PLM system in a laboratory with optical expertise [71, 81–83]. 2PLM allows measurement of both intravascular and tissue pO_2 with unprecedented spatial resolution and is well suited to imaging of pO_2 changes during functional activation [84]. Furthermore, it has been recently demonstrated that 2PLM enables estimation of blood flow in individual capillaries simultaneously with intravascular pO_2 [83].

Despite its advantages in spatial resolution and applicability to measurements of tissue oxygenation, 2PLM does not replace measurements of intrinsic signals. Rather, it complements the suite of tools available for metabolic/hemodynamic measurements. Multiple measurement techniques need to be employed to obtain the full picture of the underlying physiological process and to cross-validate one another. For example, one can combine measurements of oxygenation with extrinsic measurements of blood flow to estimate the cerebral rate of O_2 metabolism: 2PLM with optical coherence tomography [107, 108] for microscopic resolution, or intrinsic imaging with either laser speckle [66] or wide-field red blood cell velocity measurements [109] for a larger "mesoscopic" view. Below we discuss the technical aspects of the multi-wavelength CCD-based method for imaging of intrinsic signals and the application of phosphorescence quenching for imaging of intravascular and tissue pO_2, and provide specific examples and references for further reading.

2 Optical Imaging of Hemoglobin Oxygenation

Researchers have long recognized intrinsic optical changes in fluorescence, absorption, and scattering associated with neuronal and metabolic activity. The sources of fluorescence changes are small, intrinsically fluorescent metabolites such as NADH and FAD, whose signals change during a metabolic response to increased

neuronal activity or changes in O_2 availability (e.g., during hypoxia) [110]. These molecules have characteristic chromophore-specific excitation bands. The hemoglobin in blood absorbs visible light and is the main source of intrinsic contrast in brain tissue in the visible spectrum [4, 6, 25, 111–114]. At longer wavelengths, where Hb and HbO have negligible absorbance, light-scattering effects dominate. Near-infrared scattering changes, for example, underlie the contrast in optical coherence tomography [115, 116].

Since hemoglobin-based OIS was introduced to measure the functional architecture of the cortex in vivo [1], the method has been widely applied (Box 1). The popularity of OIS for in vivo studies is due largely to the robustness of the hemodynamic response, utilization of endogenous contrast agents, and moderate complexity of the optical instrumentation setup. In addition, intrinsic signals have a relatively large percentage change from the baseline ($\Delta I/I$) in response to neuronal activation, enabling data collection with minimally invasive procedures, such as imaging through the thinned skull.

Whereas OIS relies on functional hemoglobin changes to create contrast, increases in blood volume and the amount of hemoglobin during the hemodynamic response produce unwanted "artifacts" for fluorescence imaging techniques in vivo, such as calcium or NADH imaging. Absorption and scattering changes typically affect both the illuminating light on the way to the fluorophore and the emitted fluorescence. To correct the signal, one can employ algorithms based on the reflectance changes at an additional wavelength [117–119] or fluorescence signals from a physiologically inert fluorophore such as SR101 or GFP [120, 121].

OIS typically uses a CCD camera for signal detection and provides spatial resolution in the XY plane ranging from ~10 μm on the cortical surface to hundreds of micrometer in cortical layers 2–3, and no true depth resolution (see Chapter 2 in this volume). By measuring the absorption changes at multiple wavelengths of light, and given knowledge of the path length of light through the tissue, it is possible to quantify absolute hemoglobin concentration changes [38, 68]. Below we consider the quantitative estimation of Hb and HbO from multi-wavelength OIS data and the spatial resolution of common OIS instrumentation setups.

2.1 Multi-wavelength Imaging Method for Quantification of Oxy- and Deoxy-hemoglobin

Performing OIS with a number of different illumination wavelengths (referred to hereafter as "spectral" imaging) enables estimation of changes in oxy-hemoglobin (ΔHbO), deoxy-hemoglobin (ΔHb), and total hemoglobin (ΔHbT) [66–68, 122, 123]; for a recent review see [124].

For spectral imaging, one can employ a white illumination source filtered with a rotating filter wheel [9, 26, 66–68, 123, 125–127], a set of electronically controlled flashing LEDs optically chopped with appropriate filters [128], or a grating monochromator

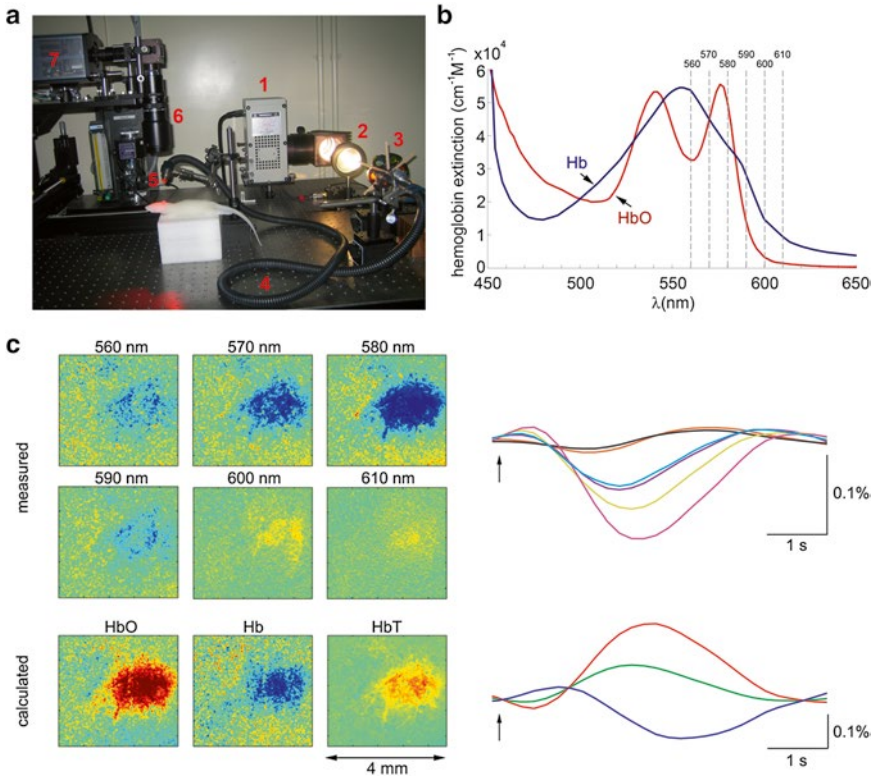

Fig. 1 Conversion of multi-wavelength signals to HbO, Hb, and HbT. (**a**) Optical instrumentation setup with a light source (*1*), focusing lens (*2*), filter wheel (*3*), fiber bundle (*4*) that brings illumination to the specimen (*5*), objective lens (*6*), and CCD camera (*7*). (**b**) Absorption spectra of hemoglobin in the visible range. (**c**) Single-filter maps of absorption changes (*left*) and the corresponding signal time-courses extracted from the active region (*right*). Signal time-courses for each of the six wavelengths are superimposed. (**d**) Estimated HbO, Hb, and HbT maps (*left*) and time-courses (*right*).

[129]. Figure 1a shows an example of a simple instrumentation setup used in our laboratory. Illuminating light (labeled "1" in the figure) from a tungsten–halogen light source (Oriel, Spectra-Physics) is directed by a lens ("2") through a 6-slot filter wheel ("3"), coupled to a 12-mm fiber bundle ("4") that brings the illuminating light to the specimen ("5"). In this filter wheel, the center wavelengths of the filters range between 560 and 610 nm at 10-nm intervals. The filter wheel is mounted on a DC motor and rotates at ~18 Hz, resulting in a ~3 Hz acquisition rate per wavelength. The light is collected by an objective lens ("6") and images are acquired by a cooled 16-bit CCD camera (Cascade 512B, Photometrics) ("7"). Image acquisition is triggered by individual filters in the filter wheel passing through an optic sensor. The image set at each wavelength is averaged across trials and the averaged data are converted to ΔHbO and ΔHb at each pixel using the modified Beer–Lambert relationship:

$$\Delta A(\lambda,t) = \left(\varepsilon_{HbO}(\lambda)\Delta C_{HbO}(t) + \varepsilon_{Hb}(\lambda)\Delta C_{Hb}(t)\right) D(\lambda) \quad (1)$$

Table 1
The pathlength correction factor and extinction coefficients for commonly used illumination wavelengths.

λ (nm)	560	570	580	590	600	610
$D(\lambda)$	0.0537	0.0500	0.0503	0.0909	0.1587	0.2044
$\varepsilon_{HbO}(\lambda)$, ×1.0e+05	0.7511	1.0247	1.1539	0.3316	0.0737	0.0346
$\varepsilon_{Hb}(\lambda)$, ×1.0e+05	1.2387	1.0380	0.8526	0.6523	0.3380	0.2174

The values for extinction coefficients are corrected for the concentration of hemoglobin in tissue.

where $\Delta A(\lambda,t) = \log(R_o/R(t))$ is the attenuation at each wavelength, R_o and $R(t)$ are the measured reflectance intensities at baseline and time t, respectively, ΔC_{HbO} and ΔC_{Hb} are the changes in concentrations of HbO and Hb, respectively, and ε_{HbO} and ε_{Hb} are the wavelength-dependent molar extinction coefficients (Fig. 1b). This equation is solved for ΔC_{HbO} and ΔC_{Hb} using a least-squares approach. The differential pathlength factor, $D(\lambda)$, accounts for the fact that each wavelength travels slightly different pathlengths through the tissue due to the wavelength dependence of scattering and absorption in the tissue. It is estimated using the approach described by Kohl et al. [38] through Monte Carlo simulations of light propagation in tissue (Table 1). Baseline concentrations of 60 and 40 μM are assumed for HbO and Hb, respectively [3, 8]. Results for relative hemoglobin changes during functional activation are only weakly sensitive to these assumed baseline values [66]. Figure 1c–d shows an example of ΔHbO/ΔHb estimation from the six-wavelength data in rat barrel cortex in response to a single deflection of one whisker. Larger hemodynamic changes induced by various pathological manipulations (e.g., middle cerebral artery occlusion, cortical spreading depression) require application of nonlinear fitting algorithms to estimate hemoglobin changes [130].

2.2 Optical Resolution and Depth Sensitivity Considerations

In two-dimensional (2D) camera-based OIS, a collimated beam in the visible spectrum incident onto the brain surface propagates inside the tissue. The reflected light from the brain is collected by the objective lens and imaged onto the CCD chip, forming a 2D image. Tissues at different depths of the cortex contribute to the image on the camera, such that the measured signal intensity of each pixel represents a weighted sum of the response through the whole depth of light penetration (with the highest sensitivity to the cortical surface) [131, 132]. Because of light scattering in the cortex, even a point source in the brain tissue will not result in an image corresponding to a diffraction-limited spot but to a much larger region. The size of this region is determined by the configuration of the optical imaging system (numerical aperture (NA) and the depth at which the image is in focus, referred to as "focal plane

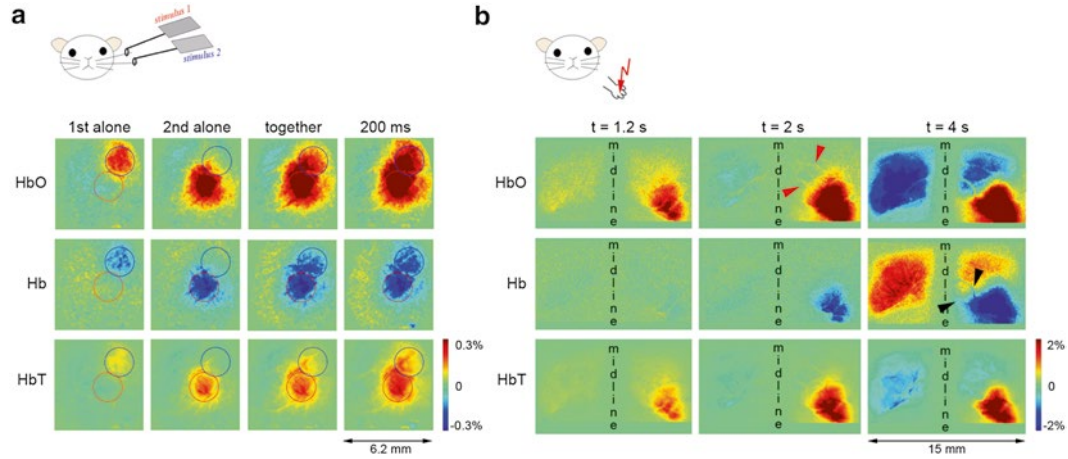

Fig. 2 Imaging of hemoglobin oxygenation in the rat primary somatosensory cortex. (**a**) Example HbO, Hb, and HbT maps in response to a tactile stimulus of single whiskers. The maps correspond to 2.5 s after the stimulus onset for four stimulus conditions: one deflection of a single whisker ("1st alone" and "2nd alone"), simultaneous deflection of both whiskers ("together"), and a sequential deflection with a 200-ms interval ("200 ms"). The signal for Hb and HbO is expressed in percent change relative to its own baseline concentration (40 and 60 μM, respectively). HbT was calculated as a sum of Hb and HbO. (**b**) Example HbO, Hb, and HbT maps in response to an electrical forepaw stimulus. *Red* and *black arrows* point to the surface arteries and veins, visible on HbO and Hb images, respectively.

depth") and the optical properties of the tissue (such as the scattering and absorption coefficients).

Propagation of light in a highly scattering medium such as cortical tissue is complicated and cannot be modeled analytically with adequate accuracy. Instead, numerical methods, such as Monte Carlo methods, are widely used to simulate light transport in tissues [133–135]. A systematic Monte Carlo study of spatial resolution and depth sensitivity for 2D optical imaging methods with configurations typically encountered in functional brain imaging demonstrated that more than 97 % of the signal comes from the top 500 μm of the tissue [134] (see Chapter 3 in this volume). Therefore, no significant contribution is expected to originate in cortical layers 4 or 5. The spatial resolution using the common NA and focal depth settings is less than or comparable to the size of cortical columns in rodent barrel cortex.

2.3 Example Application: Mapping of Rat Barrel Cortex Using Multi-wavelength Optical Imaging

OIS provides a sensitive tool for mapping the location of neuronal responses to sensory stimulation and for studying neurovascular coupling while varying the evoked hemodynamic response in the temporal and spatial domain [4, 11, 14, 48, 136]. Figure 2a shows an example from the rat barrel cortex. The skull over the barrel cortex contralateral to the stimulated whisker pad was thinned until transparent, and tactile stimuli were delivered to single whiskers at different time delays [137]. The hemodynamic response to

tactile stimulation of individual whiskers is clearly localized (red and blue circles in Fig. 2a). Moreover, one can study the additive properties of the response by stimulating multiple whiskers, either simultaneously or sequentially.

Figure 2b shows a different example of ΔHb/ΔHbO/ΔHbT maps in response to a much stronger stimulus: an electrical stimulus delivered to a forepaw in the rat. In this case, the skull was thinned bilaterally over the forepaw region of the primary somatosensory cortex. Note that the amplitude of the signal change is almost an order of magnitude larger than in the previous case. The maps in both cases have a spatial structure, which can be exploited to study the transformation of neuronal circuit activity to hemodynamic signal changes [126, 127].

3 Direct Methods for O_2 Imaging Using Phosphorescent Probes

The phosphorescence quenching method exploits exogenous molecular probes, which emit from their triplet spin states (as opposed to fluorescent probes, which emit from singlet spin states), to quantify O_2 content in living tissue [73]. O_2 can react with excited state molecules in the environment, quenching their luminescence. Collisional quenching is much less probable on the time scale of excited singlet states (nanoseconds) than of triplet states (microseconds to milliseconds), making phosphorescence much more sensitive than fluorescence to dynamic O_2 quenching. The phosphorescence decay time (τ) of a probe depends on the partial pressure of O_2 in the physiological pO_2 range according to the Stern–Volmer relationship:

$$\frac{\tau_o}{\tau} = 1 + k_q \tau_o pO_2 \qquad (2)$$

where τ_o and τ are the phosphorescence lifetimes in the absence of O_2 and at O_2 pressure pO_2, respectively, and k_q is the O_2 quenching constant. Parameters k_q and τ_o are characteristic of the probe molecule and the environment (solvent, pH, temperature, etc.) and do not depend on the measurement system. Phosphorescence quenching is arguably the most direct method of O_2 quantification, since the physics of quenching is well understood. In biological systems O_2 is the only small-molecule quencher present in sufficiently high concentrations: hence the specificity of the measurement.

Phosphorescence quenching as a form of biological oximetry has been developed specifically for in vivo applications. Phosphorescent probes (Box 2) are introduced directly into the medium of interest, where they report on the oxygenation in their local environments. External excitation and detection are used to retrieve the signal. Using phosphorescence, O_2 can be imaged in large

areas/volumes [69, 72, 138, 139] potentially in 3D [140]; no mechanical damage is done to the tissue, and the measurement can be performed with high temporal and spatial resolution. If phosphorescence is excited by ballistic photons, as in microscopy applications [141–143], the spatial resolution is limited only by the optical diffraction. Provided that the volume contains a sufficient number of probe molecules, temporal resolution is limited only by the triplet lifetime (sub-millisecond range). However, in practice, collection of multiple decays is required to obtain a reliable measurement. Thus, phosphorescent probes with high emissivity are the key to high temporal and spatial resolution.

4 Single-Photon Excitation of O_2-Sensitive Probe

Regular phosphorescence-based pO_2 measurements by linear (one-photon) excitation can be performed with relatively simple instrumentation. For example, using a time-gated CCD camera synchronized with a pulsed- or frequency-modulated excitation source [69, 70, 138, 139, 144–147], spatially resolved oxygenation maps can be collected in tissue or vasculature with temporal resolution on the order of seconds.

Frequency-modulated illumination can be provided by an optically chopped halogen source light or an LED [144, 145]. Alternatively, in the time domain, one can use flash lamps [69, 70, 138] or a pulsed laser such as a q-switched, frequency-doubled Nd:YAG laser that delivers ~6-ns pulses at a fixed frequency (10 Hz) [139, 147]. As with OIS, the excitation light is typically coupled into a multimode fiber positioned at an angle relatively oblique to the cortical surface. The sample can also be excited with a 0° incidence angle if a dichroic mirror is used to couple the excitation and detection beams. In a wide-field microscopy system operating in one of our laboratories [139], the phosphorescence light is collected by a low-magnification infinity-corrected objective (e.g., Olympus XL Fluor 4x/340, 0.28 NA), and an image is formed on the CCD sensor by a 100-mm focal length tube lens. A long-pass filter is positioned between the objective and the tube lens to suppress the excitation light, and the signal is detected from the entire field of view at once. Higher signal-to-noise ratio (SNR) can be achieved by binning pixels on the CCD chip (at a price of lower spatial resolution). A single lifetime image (reconstruction of the phosphorescent decay) requires multiple camera exposures temporally jittered relative to the illumination. Using a pulsed laser source, each camera exposure starts at a specific programmed delay with respect to its corresponding excitation pulse (Fig. 3a). For each pixel, intensity values are plotted against the delay between the excitation pulse and CCD exposure to generate the phosphorescence decay. If frequency-modulated

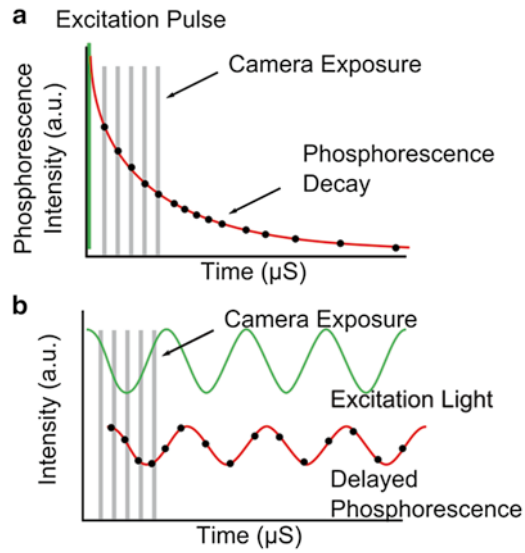

Fig. 3 Phosphorescence lifetime measurements—time-domain and frequency-domain methods. (**a**) Timing relationship for time-domain measurement of phosphorescence decay. A pulsed laser delivers light at a fixed repetition rate, with each pulse generating a phosphorescent decay. Each laser pulse triggers a corresponding brief camera exposure, delayed by a programmed period after the laser pulse. Each camera exposure captures a different portion of the phosphorescence decay. After several laser pulses, the phosphorescence decay can be measured and the lifetime is estimated by an exponential fit. (**b**) Timing relationship for frequency-domain lifetime measurement. A sinusoidally modulated excitation beam runs continuously, and a synchronized camera collects multiple brief exposures at programmed phase delays. After several exposures, the delayed sinusoidal phosphorescence waveform can be estimated, and the lifetime is estimated by $\tan(\theta)/2\pi \times$ modulation frequency, where theta is the phase delay of the phosphorescence waveform [98].

excitation is used rather than pulsed excitation, the lifetime can be computed from the phosphorescence waveform's phase delay with respect to the excitation waveform (Fig. 3b) [145]. Maps of pO_2 are computed per pixel using the Stern–Volmer relationship (Eq. 2).

An illustration of CCD-based intravascular pO_2 imaging is presented in Fig. 4. In this example, a simple laser speckle imaging system was used simultaneously with the pO_2 measurement to record relative blood flow changes (rCBF) for estimation of the cerebral metabolic rate of O_2 ($CMRO_2$) [139]. See Chapter 15 in this volume for review of laser speckle imaging.

As discussed in Sect. 2.2, CCD-based imaging (in combination with wide-field excitation of the phosphor) suffers from poor spatial resolution due to the scattering of light in tissue. Confocal microscopy can be employed to improve the spatial resolution in a single-photon excitation mode [143]. In the confocal regime, the scanning galvanometer mirrors can be programmed to direct the

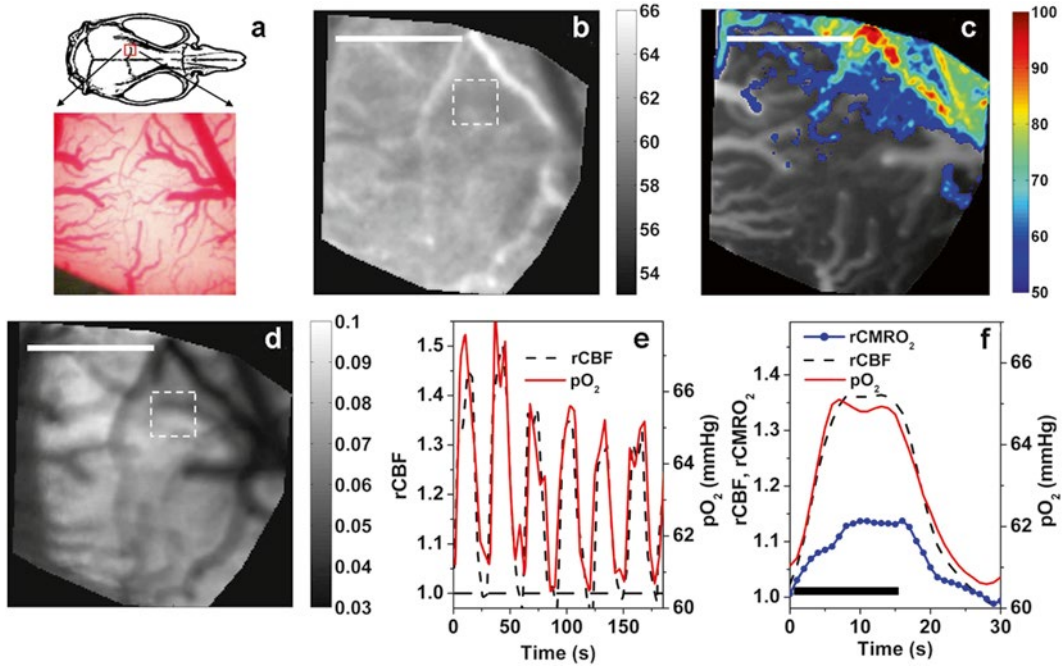

Fig. 4 CCD measurement of intravascular pO_2 with simultaneous laser speckle imaging during forepaw stimulation. (**a**) Position of the cranial window over the forepaw area of the somatosensory cortex and a photograph of the cortical vasculature. (**b**) Baseline pO_2 map. (**c**) Composite image consisting of phosphorescence intensity (*gray*) and activation area (*color*). (**d**) Baseline speckle contrast image. (**e**) Time-courses of pO_2 (*red solid curve*) and rCBF (*black dashed curve*) during several stimulation sequences extracted from the ROI marked by the *white rectangles* in (**b**) and (**d**). *Black horizontal bars* in (**e**) and (**f**) denote stimulus duration. (**f**) Trial-averaged pO_2, rCBF, and $rCMRO_2$ responses. Scale bar is 1 mm.

excitation beam to distinct locations from which pO_2 measurements are made. The detected light must be de-scanned by placing the detector after the galvanometer scanners and spatially filtered using a pinhole in front of the detector. Thus, spatial resolution is improved by (1) confining the excitation to a small volume and (2) rejecting out-of-focus phosphorescence by implementing the pinhole.

5 Two-Photon Phosphorescence Lifetime Imaging (2PLM) of O_2

In addition to single-photon excitation of O_2-sensitive probes, two-photon excitation is now being employed to achieve better depth resolution and higher spatial localization [71, 81–83, 148]. In two-photon microscopy, ultrashort laser pulses and a high NA objective are required to induce nonlinear excitation of the probe, confining the generation of the excited state to the immediate vicinity of the focal volume. In two-photon microscopes constructed in our laboratories [81, 82], phosphorescence is excited by trains of femtosecond pulses from a Ti:sapphire oscillator, gated

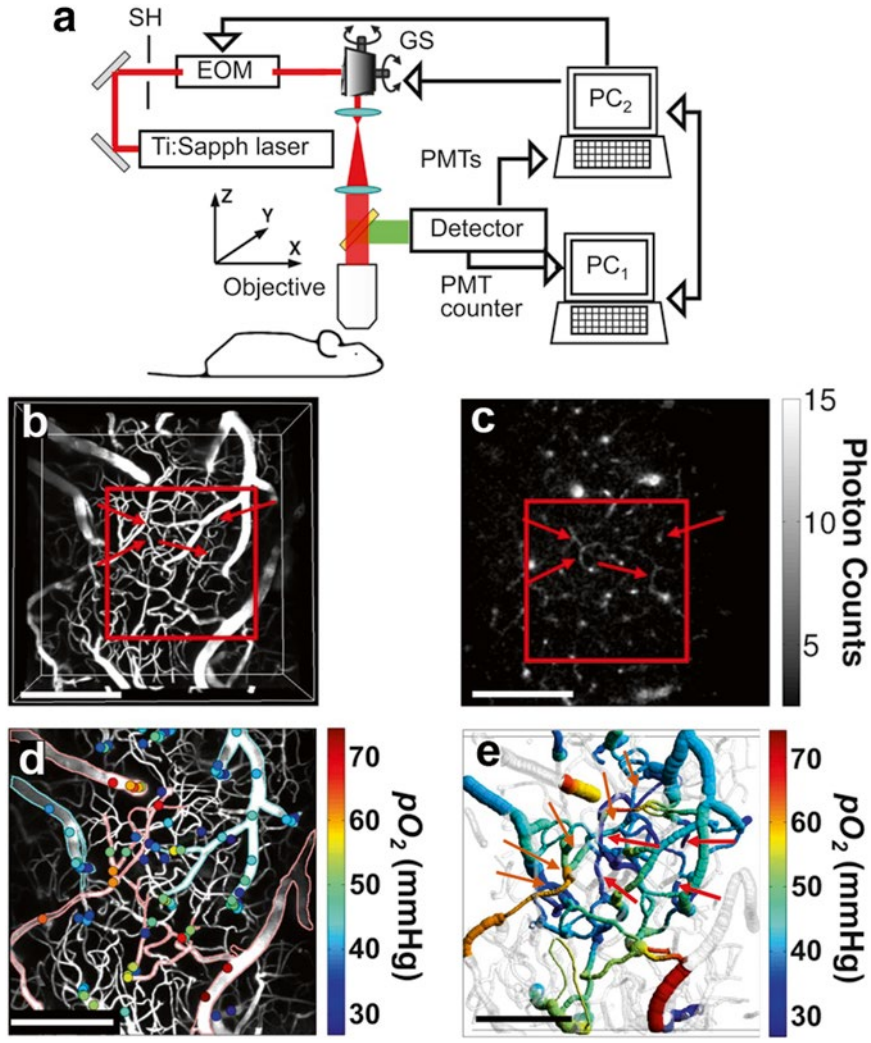

Fig. 5 Two-photon detection of phosphorescence. (**a**) Schematic of the experimental setup. *EOM* electro-optic modulator, *GS* galvanometer scanner, *PMTs* analog-mode photomultiplier tubes, *PMT counter* a Geiger-mode photomultiplier tube. (**b**) Maximum intensity projection along the *z* direction of a 250-μm-thick stack in the mouse cortex. The vasculature was labeled with dextran-conjugated fluorescein isothiocyanate (FITC). (**c**) Phosphorescence intensity image of microvasculature obtained at a depth of 240 μm below the cortical surface. The *color bar* shows the average number of photon counts in each pixel collected during a single phosphorescence decay. Four *arrows* mark the locations of the same capillary vessels in panels (**b**), (**c**), and (**e**). (**d**) Measured pO_2 values in microvasculature at various depths (*colored dots*), overlaid on the maximum intensity projection image of vasculature structure (grayscale). Digital processing was performed to remove images of the dura vessels. Edges of the major pial arterioles and venules are outlined in *red* and *blue*, respectively. (**e**) Composite image showing a projection of the imaged vasculature stack. *Red arrows* mark pO_2 measurement locations in the capillary vessels at a depth of 240 μm. *Orange arrows* point to the consecutive branches of the vascular tree, from pial arteriole (*bottom left arrow*) to the capillary and then to the connection with ascending venule (*top right arrow*). Scale bar, 200 μm.

by an electro-optic modulator. The phosphorescent signals are detected by photon-counting modules (Fig. 5a). For example, the probe can be excited by a 10-μs excitation gate, followed by a 300-μs data acquisition period. The counts are binned and subsequently used to reconstruct the decay, which is analyzed by the least-squares method to obtain the phosphorescence lifetime. The SNR of the measurement is determined solely by the number of the counted photons. Only very few photons can be collected from a near diffraction-limited volume per excitation gate at a reasonable probe concentration [81]. Therefore, decays are typically analyzed after averaging multiple excitation cycles. The size of the excitation volume is dependent on the laser power and the duration of the excitation gate [148]. These parameters can be adjusted to select the optimal combination of the excitation volume (spatial resolution) and pixel dwell time (temporal resolution). For example, to measure baseline pO_2 in the mouse cortex we usually acquire 500–2,000 excitation cycles per point using PtP-C343 (for description of this and other probes see [74, 75, 77, 80–81]) at intravascular concentration of <15 μM and with 10-μs excitation gates. The average laser power during the excitation gate is <10 mW at the focal plane. Using 2,000 cycles, a grid of 600 points can be acquired in ~6 min. We estimate that under this excitation regime the emitting volume has ~2 μm lateral (XY) and ~5 μm axial (Z) dimensions.

Using 2PLM in an upright setup [82], we can image the cortex of anesthetized mice and rats through sealed cranial windows, either injecting the phosphorescence probe into the vasculature through the femoral artery or pressure-injecting it directly into the brain tissue. Structural images of the cortical vasculature can be obtained either by imaging fluorescence emission from coumarin-343 (C343) chromophores constituting the two-photon antenna of the PtP-C343 probe or, to increase contrast, by using intravenously administered fluorescein isothiocyanate (FITC) conjugated with dextran (Fig. 5b).

O_2 imaging in the cerebral cortex is typically performed in two steps. First, we raster-scan the excitation beam over the field of view, rendering 2D survey maps of the integrated emission intensity (150×150 or 250×250 pixels, acquired in ~9 or ~25 s, respectively). A single-plane scan performed 240 μm below the brain surface in Fig. 5c demonstrates the ability of the system to resolve the structure of the microvasculature down to the capillary level. After mapping the tissue, we average multiple excitation cycles in selected locations for accurate pO_2 determination. Given the average of 500–2,000 cycles, the acquisition time corresponds to a temporal resolution of 0.16–0.76 s per single-point pO_2 measurement. Finally, using Stern–Volmer calibration plots (Eq. 2), we convert phosphorescence lifetimes, obtained by fitting, into pO_2 values (Fig. 5d–e).

5.1 Example Application: Two-Photon Imaging of Tissue pO_2 Dynamics in Rat Somatosensory Cortex with Phosphorescent Nanoprobe PtP-C343

Measurement of pO_2 based on 2PLM is uniquely capable of assessing pO_2 directly in the cortical tissue. In the example shown in Fig. 6, PtP-C343 was microinjected into the interstitial space (tissue) of the rat primary somatosensory cortex through a glass pipette attached to a pressure injector, as is usually done with calcium indicators [149]. In contrast to calcium indicators, PtP-C343 is easily dissolved in artificial cerebrospinal fluid and does not require additional solvents (such as pluronic acid or DMSO). Following microinjection, PtP-C343 quickly diffuses within ~1 mm from the injection site. Using our protocol, there is no significant decrease in the signal intensity up to 4 h after the injection. After that, the signal slowly reduces. Thus, a single injection per subject is sufficient. FITC is administered intravenously to delineate the vasculature (Fig. 6a) and allows coregistration of pO_2 measurements relative to the vascular O_2 sources. To investigate the spatial distribution of tissue pO_2 at the baseline (resting) level of neuronal activity, one can acquire grids of points (Fig. 6b). Plotted as a function of the radial distance from the arteriole (Fig. 6c), these data demonstrate a gradient indicating that O_2 diffuses into the tissue through the walls of diving arterioles [84].

When the probe is also injected intravenously, one can perform simultaneous intravascular and tissue pO_2 measurements. However, given the resolution of $\sim 2 \times 2 \times 5$ μm, capillary signals cannot be resolved if the probe is present in both intra- and extravascular compartments. Nevertheless, one can resolve intravascular pO_2 in diving arterioles, although the ontogeny of the signal at the vessel border would be uncertain (Fig. 6d). Alternatively, capillary pO_2 can be readily imaged if the probe is present only in the vasculature (but not in the tissue around it) as demonstrated in Fig. 5.

When the beam is moved from point to point, a short time period is required to stabilize the galvanometer mirrors. Therefore, the most time-efficient way to accomplish a point pO_2 measurement is to stay at the same point and collect multiple decays before moving to the next point. For functional measurements, however, the sampling rate per point must match the kinetics of the dynamic process to be imaged. Figure 7 shows an example of a dynamic pO_2 measurement performed at ~1 Hz. In this example, 50 decays were collected at each point and the number of points was adjusted to allow us to revisit the point within ~1 s (1 Hz sampling rate). Therefore, after determining the target acquisition speed, one has to compromise between the overall number of measurement points and the number of excitation cycles collected per point. Multiple stimulus trials can be averaged before fitting for the decay to increase the SNR of the measurement. For example, 20 trials were averaged in Fig. 7.

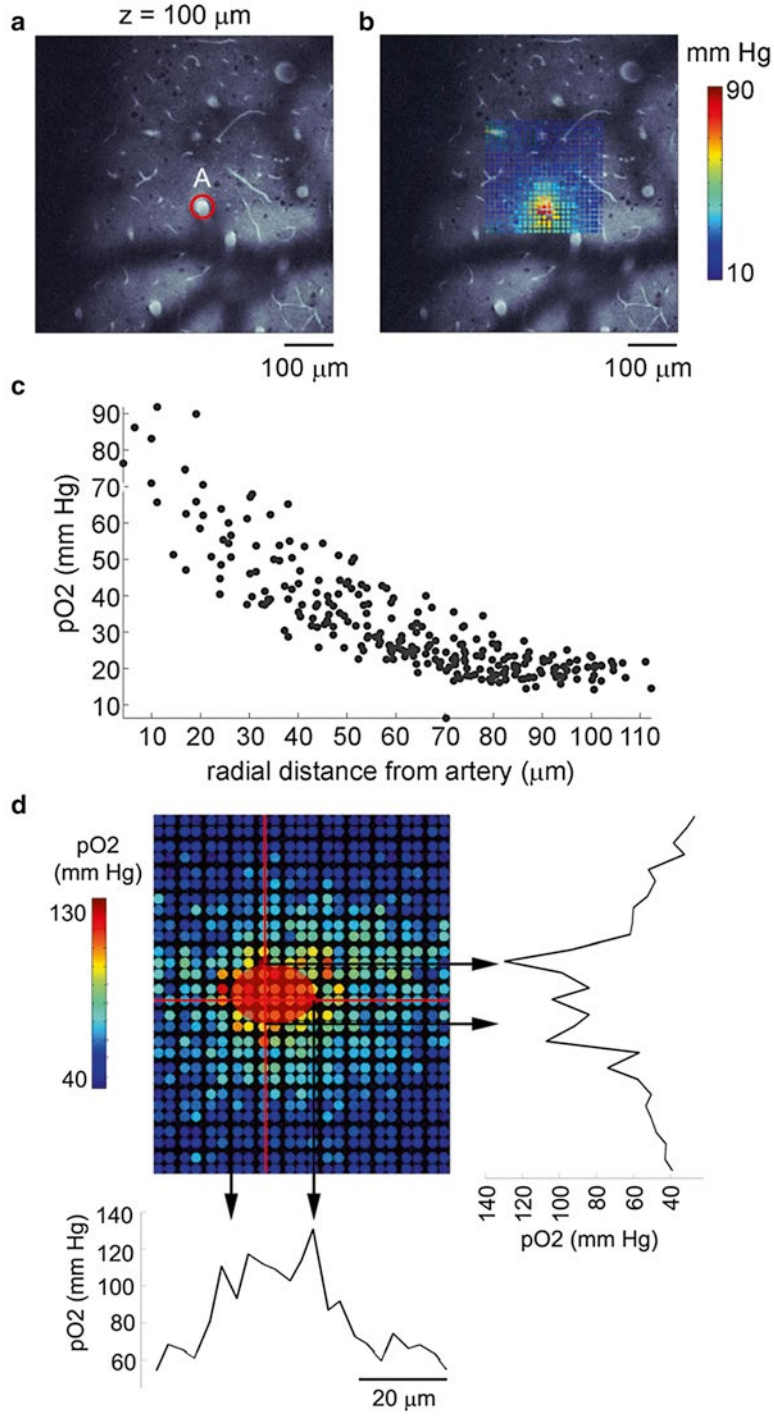

Fig. 6 Spatial distribution of baseline pO_2 values. (**a**) A reference vascular image with an arteriole ("A"). The fluorescent contrast is due to intravascular FITC. The background fluorescence is due to the excitation of coumarin molecules in PtP-C343. (**b**) The same image as in (**a**) with superimposed pO_2 values and segmented arteriolar territory. (**c**) pO_2 as a function of the radial distance from the arteriole. (**d**) The plots at the *bottom* and on the *right* show *X* and *Y* profiles cut through the *red lines* in the image. The *red circle* indicates the arteriolar boundary estimated from the FITC reference.

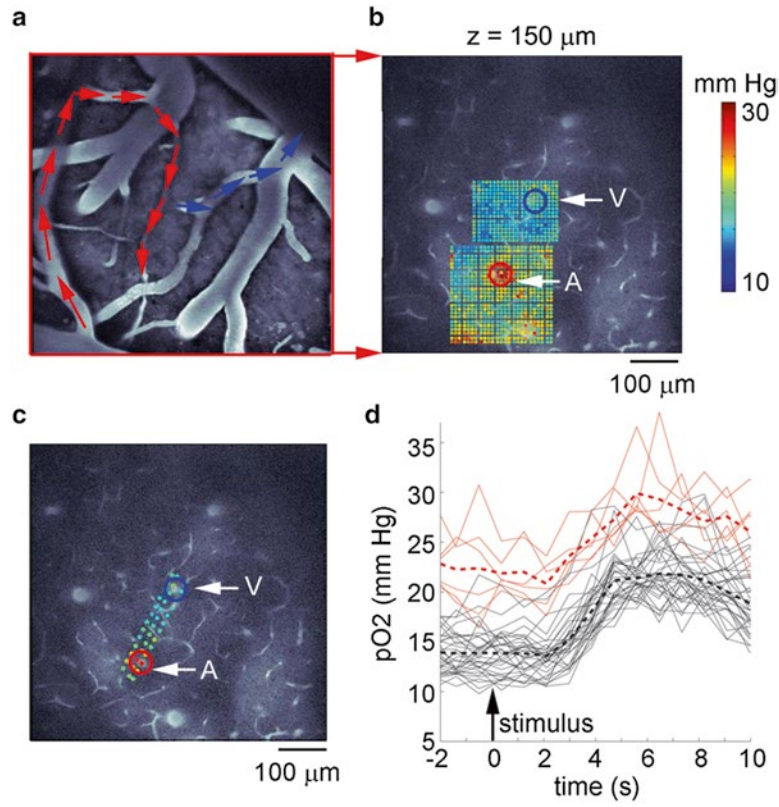

Fig. 7 Stimulus-induced tissue pO_2 changes in rat primary somatosensory cortex. (**a**) An image of the surface vasculature calculated as a maximum intensity projection (MIP) of an image stack 0–100 μm in depth using a 4× objective. Individual images were acquired every 10 μm. (**b**) The same region at the depth plane of pO_2 measurements, 150 μm below the surface. "A" and "V" indicate a diving arteriole and a surfacing venule, respectively. *Red* and *blue arrows* in (**a**) show the upstream and downstream surface arteriole and venule for "A" and "V," respectively. A grid of measured baseline pO_2 values is superimposed on the vascular reference plane. (**c**) The same vascular reference plane as in (**b**) with superimposed pO_2 measurement points used for dynamic measurements. The points are color-coded according to the baseline pO_2. (**d**) Stimulus-evoked time-courses of pO_2 change, extracted from each of the measurement points in (**c**). The traces are divided into two categories: high baseline (*red*) and low baseline (*black*). The *dotted red* and *black lines* correspond to the average for each category. The *black arrow* denotes stimulus onset.

One additional limitation of 2PLM measurements is a decrease in SNR with increasing baseline pO_2. This limitation stems directly from the O_2 sensing mechanism of the probe: quenching of the triplet state by O_2 leads to a fewer emitted photons. At higher pO_2s, more of the probe molecules are quenched, resulting in fewer photons reaching the detector. The decrease in SNR at high pO_2 is usually not a problem for baseline measurements, where it can be compensated for by averaging more excitation cycles per point.

6 Conclusions and Outlook

In this chapter we have reviewed methods for measuring intravascular and tissue oxygenation, with a particular focus on applying OIS and phosphorescence quenching in the cerebral cortex. In the context of cortical function, these methods on their own provide a somewhat one-sided view of a single (but very important) aspect of the underlying physiological processes—oxygenation. A more complete picture can be obtained by combining these imaging modalities with other measurements of neuronal, glial, vascular, and metabolic activity. As such, OIS can be readily combined with simultaneous electrophysiological recordings [9, 27, 67, 150] or fMRI [105], and can serve as a bridge between the neuronal and fMRI signals, getting around the need to filter electrical potentials recorded in the environment of changing electromagnetic fields. Likewise, 2PLM can be combined with optical imaging of neuronal activity (e.g., two-photon calcium imaging [152], at least in alternating stimulus trials; see Chapter 9 in this volume) and optical coherence tomography measurements of blood flow [107, 108]. Measurements of capillary flow—the speed of red blood cells in individual capillaries—can be extracted directly from 2PLM data when a phosphorescent O_2 probe is applied intravascularly [83].

The choice of method for measuring oxygenation would depend on the requirement for spatial resolution, compartments of interest (intravascular or tissue), allocated budget, and availability of optical engineering expertise. OIS remains the method of choice for "mesoscopic" mapping of neuronal activity on the cortical surface: It does not require delivery of extrinsic probes and is inexpensive and easy to implement in a standard neuroscience laboratory setting. The most significant drawbacks of OIS are scattering and lack of depth resolution, which result in an inherent uncertainty in the spatial origin of the imaged signals. 2PLM is situated on the opposite side of the experimental/instrumentation complexity spectrum, but offers high-resolution, deep-penetration imaging of either intra- or extravascular pO_2, depending on the location of the pO_2 probe. Confocal imaging might serve as a good compromise on the instrumentation side and does not require probes with high two-photon cross sections, offering more flexibility in the choice of probe molecules. In the two-photon regime, the most important parameter determining the temporal and spatial resolution of the measurement is the phosphorescence quantum yield of the probe. Probes based on metalloporphyrins and other chromophores exhibiting brighter phosphorescence are currently being developed. Likewise, strategies for intracellular delivery of phosphorescent O_2 probes are under investigation. In combination with transgenic methods for identification of specific neuronal cell types in the cerebral cortex, intracellular O_2 probes could be used for evaluation of cell-type specific pathology in neurodegenerative disease.

Acknowledgements

We gratefully acknowledge support from the NINDS (NS051188 and NS057198 to A.D., NS057476 and NS055104 to D.A.B.), NIBIB (EB00790 to A.M.D., EB009118 to A.D., EB2066 to B.R.R., EB007279 to S.A.V.), American Heart Association Grant No. 11SDG7600037 to S.S., and NIH SIG S10-RR022428 to D.A.B.

References

1. Grinvald A, Lieke E, Frostig RD, Gilbert CD, Wiesel TN (1986) Functional architecture of cortex revealed by optical imaging of intrinsic signals. Nature 324:361–364
2. Berwick J, Martin C, Martindale J, Jones M, Johnston D, Zheng Y, Redgrave P, Mayhew J (2002) Hemodynamic response in the unanesthetized rat: intrinsic optical imaging and spectroscopy of the barrel cortex. J Cereb Blood Flow Metab 22:670–679
3. Jones M, Berwick J, Mayhew J (2002) Changes in blood flow, oxygenation, and volume following extended stimulation of rodent barrel cortex. Neuroimage 15:474–487
4. Frostig RD, Lieke EE, Ts'o DY, Grinvald A (1990) Cortical functional architecture and local coupling between neuronal activity and the microcirculation revealed by in vivo high-resolution optical imaging of intrinsic signals. Proc Natl Acad Sci USA 87: 6082–6086
5. Malonek D, Dirnagl U, Lindauer U, Yamada K, Kanno I, Grinvald A (1997) Vascular imprints of neuronal activity: relationships between the dynamics of cortical blood flow, oxygenation, and volume changes following sensory stimulation. Proc Natl Acad Sci USA 94:14826–14831
6. Malonek D, Grinvald A (1996) Interactions between electrical activity and cortical microcirculation revealed by imaging spectroscopy: implications for functional brain mapping. Science 272:551–554
7. Martindale J, Mayhew J, Berwick J, Jones M, Martin C, Johnston D, Redgrave P, Zheng Y (2003) The hemodynamic impulse response to a single neural event. J Cereb Blood Flow Metab 23:546–555
8. Mayhew J, Johnston D, Berwick J, Jones M, Coffey P, Zheng Y (2000) Spectroscopic analysis of neural activity in brain: increased oxygen consumption following activation of barrel cortex. Neuroimage 12:664–675
9. Nemoto M, Sheth S, Guiou M, Pouratian N, Chen JW, Toga AW (2004) Functional signal- and paradigm-dependent linear relationships between synaptic activity and hemodynamic responses in rat somatosensory cortex. J Neurosci 24:3850–3861
10. Sheth S, Nemoto M, Guiou M, Walker M, Pouratian N, Toga AW (2003) Evaluation of coupling between optical intrinsic signals and neuronal activity in rat somatosensory cortex. Neuroimage 19:884–894
11. Vanzetta I, Hildesheim R, Grinvald A (2005) Compartment-resolved imaging of activity-dependent dynamics of cortical blood volume and oximetry. J Neurosci 25:2233–2244
12. Chen G, Lu HD, Roe AW (2008) A map for horizontal disparity in monkey V2. Neuron 58:442–450
13. Erinjeri JP, Woolsey TA (2002) Spatial integration of vascular changes with neural activity in mouse cortex. J Cereb Blood Flow Metab 22:353–360
14. Shtoyerman E, Arieli A, Slovin H, Vanzetta I, Grinvald A (2000) Long-term optical imaging and spectroscopy reveal mechanisms underlying the intrinsic signal and stability of cortical maps in V1 of behaving monkeys. J Neurosci 20:8111–8121
15. Sirotin YB, Das A (2009) Anticipatory haemodynamic signals in sensory cortex not predicted by local neuronal activity. Nature 457:475–479
16. Roy CS, Sherrington CS (1890) On the regulation of the blood-supply of the brain. J Physiol 11:85–158
17. Fox PT, Raichle ME (1984) Stimulus rate dependence of regional cerebral blood flow in human striate cortex, demonstrated by positron emission tomography. J Neurophysiol 51:1109–1120
18. Lassen NA, Ingvar DH (1961) The blood flow of the cerebral cortex determined by radioactive krypton. Experientia 17:42–43
19. Sokoloff L, Reivich M, Kennedy C, Des Rosiers MH, Patlak CS, Pettigrew KD,

Sakurada O, Shinohara M (1977) The [14C] deoxyglucose method for the measurement of local cerebral glucose utilization: theory, procedure, and normal values in the conscious and anesthetized albino rat. J Neurochem 28:897–916

20. Sokoloff L (1981) Localization of functional activity in the central nervous system by measurement of glucose utilization with radioactive deoxyglucose. J Cereb Blood Flow Metab 1:7–36
21. Penfield W (1933) The evidence for a cerebral vascular mechanism in epilepsy. Ann Intern Med 7:303–310
22. Jobsis FF (1977) Noninvasive, infrared monitoring of cerebral and myocardial oxygen sufficiency and circulatory parameters. Science 198:1264–1267
23. Chance B, Cohen P, Jobsis F, Schoener B (1962) Intracellular oxidation-reduction states in vivo. Science 137:499–508
24. Vanzetta I, Slovin H, Omer DB, Grinvald A (2004) Columnar resolution of blood volume and oximetry functional maps in the behaving monkey; implications for FMRI. Neuron 42:843–854
25. Vanzetta I, Grinvald A (1999) Increased cortical oxidative metabolism due to sensory stimulation: implications for functional brain imaging. Science 286:1555–1558
26. Sheth SA, Nemoto M, Guiou MW, Walker MA, Toga AW (2005) Spatiotemporal evolution of functional hemodynamic changes and their relationship to neuronal activity. J Cereb Blood Flow Metab 25:830–841
27. Sheth SA, Nemoto M, Guiou M, Walker M, Pouratian N, Toga AW (2004) Linear and nonlinear relationships between neuronal activity, oxygen metabolism, and hemodynamic responses. Neuron 42:347–355
28. Buxton RB (2001) The elusive initial dip. Neuroimage 13:953–958
29. Lindauer U, Royl G, Leithner C, Kuhl M, Gold L, Gethmann J, Kohl-Bareis M, Villringer A, Dirnagl U (2001) No evidence for early decrease in blood oxygenation in rat whisker cortex in response to functional activation. Neuroimage 13:988–1001
30. Sirotin YB, Hillman EM, Bordier C, Das A (2009) Spatiotemporal precision and hemodynamic mechanism of optical point spreads in alert primates. Proc Natl Acad Sci USA 106:18390–18395
31. Vanzetta I, Grinvald A (2001) Evidence and lack of evidence for the initial dip in the anesthetized rat: implications for human functional brain imaging. Neuroimage 13:959–967
32. Harel N, Mori N, Sawada S, Mount RJ, Harrison RV (2000) Three distinct auditory areas of cortex (AI, AII, and AAF) defined by optical imaging of intrinsic signals. Neuroimage 11:302–312
33. Spitzer MW, Calford MB, Clarey JC, Pettigrew JD, Roe AW (2001) Spontaneous and stimulus-evoked intrinsic optical signals in primary auditory cortex of the cat. J Neurophysiol 85:1283–1298
34. Versnel H, Mossop JE, Mrsic-Flogel TD, Ahmed B, Moore DR (2002) Optical imaging of intrinsic signals in ferret auditory cortex: responses to narrowband sound stimuli. J Neurophysiol 88:1545–1558
35. Chen-Bee CH, Agoncillo T, Xiong Y, Frostig RD (2007) The triphasic intrinsic signal: implications for functional imaging. J Neurosci 27:4572–4586
36. Sheth SA, Nemoto M, Guiou M, Walker M, Pouratian N, Hageman N, Toga AW (2004) Columnar specificity of microvascular oxygenation and volume responses: implications for functional brain mapping. J Neurosci 24: 634–641
37. Mc Loughlin NP, Blasdel GG (1998) Wavelength-dependent differences between optically determined functional maps from macaque striate cortex. Neuroimage 7:326–336
38. Kohl M, Lindauer U, Royl G, Kuhl M, Gold L, Villringer A, Dirnagl U (2000) Physical model for the spectroscopic analysis of cortical intrinsic optical signals. Phys Med Biol 45: 3749–3764
39. Bosking WH, Zhang Y, Schofield B, Fitzpatrick D (1997) Orientation selectivity and the arrangement of horizontal connections in tree shrew striate cortex. J Neurosci 17:2112–2127
40. Lu HD, Chen G, Tanigawa H, Roe AW (2010) A motion direction map in macaque V2. Neuron 68:1002–1013
41. Ts'o DY, Frostig RD, Lieke EE, Grinvald A (1990) Functional organization of primate visual cortex revealed by high resolution optical imaging. Science 249:417–420
42. Ts'o DY, Roe AW, Gilbert CD (2001) A hierarchy of the functional organization for color, form and disparity in primate visual area V2. Vision Res 41:1333–1349
43. Malonek D, Tootell RB, Grinvald A (1994) Optical imaging reveals the functional architecture of neurons processing shape and motion in owl monkey area MT. Proc Biol Sci 258:109–119
44. Tanigawa H, Lu HD, Roe AW (2010) Functional organization for color and orientation in macaque V4. Nat Neurosci 13: 1542–1548

45. Wang G, Tanaka K, Tanifuji M (1996) Optical imaging of functional organization in the monkey inferotemporal cortex. Science 272: 1665–1668
46. Kalatsky VA, Polley DB, Merzenich MM, Schreiner CE, Stryker MP (2005) Fine functional organization of auditory cortex revealed by Fourier optical imaging. Proc Natl Acad Sci USA 102:13325–13330
47. Bakin JS, Kwon MC, Masino SA, Weinberger NM, Frostig RD (1996) Suprathreshold auditory cortex activation visualized by intrinsic signal optical imaging. Cereb Cortex 6: 120–130
48. Masino SA, Kwon MC, Dory Y, Frostig RD (1993) Characterization of functional organization within rat barrel cortex using intrinsic signal optical imaging through a thinned skull. Proc Natl Acad Sci USA 90: 9998–10002
49. Chen LM, Friedman RM, Ramsden BM, LaMotte RH, Roe AW (2001) Fine-scale organization of SI (area 3b) in the squirrel monkey revealed with intrinsic optical imaging. J Neurophysiol 86:3011–3029
50. Chen LM, Friedman RM, Roe AW (2003) Optical imaging of a tactile illusion in area 3b of the primary somatosensory cortex. Science 302:881–885
51. Shoham D, Grinvald A (2001) The cortical representation of the hand in macaque and human area S-I: high resolution optical imaging. J Neurosci 21:6820–6835
52. Chen LM, Friedman RM, Roe AW (2009) Area-specific representation of mechanical nociceptive stimuli within SI cortex of squirrel monkeys. Pain 141:258–268
53. Grinvald A, Frostig RD, Siegel RM, Bartfeld E (1991) High-resolution optical imaging of functional brain architecture in the awake monkey. Proc Natl Acad Sci USA 88: 11559–11563
54. Vnek N, Ramsden BM, Hung CP, Goldman-Rakic PS, Roe AW (1999) Optical imaging of functional domains in the cortex of the awake and behaving monkey. Proc Natl Acad Sci USA 96:4057–4060
55. Arieli A, Grinvald A, Slovin H (2002) Dural substitute for long-term imaging of cortical activity in behaving monkeys and its clinical implications. J Neurosci Methods 114:119–133
56. Chen LM, Heider B, Williams GV, Healy FL, Ramsden BM, Roe AW (2002) A chamber and artificial dura method for long-term optical imaging in the monkey. J Neurosci Methods 113:41–49
57. Chapman B, Stryker MP, Bonhoeffer T (1996) Development of orientation preference maps in ferret primary visual cortex. J Neurosci 16:6443–6453
58. Godecke I, Kim DS, Bonhoeffer T, Singer W (1997) Development of orientation preference maps in area 18 of kitten visual cortex. Eur J Neurosci 9:1754–1762
59. Lowel S, Schmidt KE, Kim DS, Wolf F, Hoffsummer F, Singer W, Bonhoeffer T (1998) The layout of orientation and ocular dominance domains in area 17 of strabismic cats. Eur J Neurosci 10:2629–2643
60. Schmidt KE, Singer W, Galuske RA (2004) Processing deficits in primary visual cortex of amblyopic cats. J Neurophysiol 91:1661–1671
61. Schwartz TH, Bonhoeffer T (2001) In vivo optical mapping of epileptic foci and surround inhibition in ferret cerebral cortex. Nat Med 7:1063–1067
62. Zhao M, Suh M, Ma H, Perry C, Geneslaw A, Schwartz TH (2007) Focal increases in perfusion and decreases in hemoglobin oxygenation precede seizure onset in spontaneous human epilepsy. Epilepsia 48:2059–2067
63. Pouratian N, Cannestra AF, Martin NA, Toga AW (2002) Intraoperative optical intrinsic signal imaging: a clinical tool for functional brain mapping. Neurosurg Focus 13:e1
64. Toga AW, Cannestra AF, Black KL (1995) The temporal/spatial evolution of optical signals in human cortex. Cereb Cortex 5: 561–565
65. Eaton WA, Henry ER, Hofrichter J, Mozzarelli A (1999) Is cooperative oxygen binding by hemoglobin really understood? Nat Struct Biol 6:351–358
66. Dunn AK, Devor A, Dale AM, Boas DA (2005) Spatial extent of oxygen metabolism and hemodynamic changes during functional activation of the rat somatosensory cortex. Neuroimage 27:279–290
67. Devor A, Dunn AK, Andermann ML, Ulbert I, Boas DA, Dale AM (2003) Coupling of total hemoglobin concentration, oxygenation, and neural activity in rat somatosensory cortex. Neuron 39:353–359
68. Dunn AK, Devor A, Bolay H, Andermann ML, Moskowitz MA, Dale AM, Boas DA (2003) Simultaneous imaging of total cerebral hemoglobin concentration, oxygenation, and blood flow during functional activation. Opt Lett 28:28–30
69. Wilson DF, Pastuszko A, DiGiacomo JE, Pawlowski M, Schneiderman R, Delivoria-Papadopoulos M (1991) Effect of hyperventila-

tion on oxygenation of the brain cortex of newborn piglets. J Appl Physiol 70:2691–2696

70. Wilson DF, Gomi S, Pastuszko A, Greenberg JH (1993) Microvascular damage in the cortex of cat brain from middle cerebral artery occlusion and reperfusion. J Appl Physiol 74: 580–589
71. Estrada AD, Ponticorvo A, Ford TN, Dunn AK (2008) Microvascular oxygen quantification using two-photon microscopy. Opt Lett 33:1038–1040
72. Rumsey WL, Vanderkooi JM, Wilson DF (1988) Imaging of phosphorescence: a novel method for measuring oxygen distribution in perfused tissue. Science 241:1649–1651
73. Vanderkooi JM, Maniara G, Green TJ, Wilson DF (1987) An optical method for measurement of dioxygen concentration based upon quenching of phosphorescence. J Biol Chem 262:5476–5482
74. Lebedev AY, Cheprakov AV, Sakadzic S, Boas DA, Wilson DF, Vinogradov SA (2009) Dendritic phosphorescent probes for oxygen imaging in biological systems. ACS Appl Mater Interfaces 1:1292–1304
75. Vinogradov SA, Wilson DF (2011) Porphyrin-dendrimers as biological oxygen sensors. In: Campagna S, Ceroni P, Puntoriero F (eds) Designing dendrimers. Wiley, New York
76. Vinogradov SA, Wilson DF (1995) Metallotetrabenzoporphyrins. New phosphorescent probes for oxygen measurements. J Chem Soc Perkin Trans 2:103–111
77. Vinogradov SA, Lo LW, Wilson DF (1999) Dendritic polyglutamic porphyrins: probing porphyrin protection by oxygen-dependent quenching of phosphorescence. Chem Eur J 5:1338–1347
78. Rietveld IB, Kim E, Vinogradov SA (2003) Dendrimers with tetrabenzoporphyrin cores: near infrared phosphors for in vivo oxygen imaging. Tetrahedron 59:3821–3831
79. Dunphy I, Vinogradov SA, Wilson DF (2002) Oxyphor R2 and G2: phosphors for measuring oxygen by oxygen-dependent quenching of phosphorescence. Anal Biochem 310: 191–198
80. Lebedev AY, Troxler T, Vinogradov SA (2008) Design of metalloporphyrin-based dendritic nanoprobes for two-photon microscopy of oxygen. J Porphyr Phthalocyanines 12:1261–1269
81. Finikova OS, Lebedev AY, Aprelev A, Troxler T, Gao F, Garnacho C, Muro S, Hochstrasser RM, Vinogradov SA (2008) Oxygen microscopy by two-photon-excited phosphorescence. Chemphyschem 9:1673–1679
82. Sakadzic S, Roussakis E, Yaseen MA, Srinivasan VJ, Mandeville ET, Devor A, Lo EH, Vinogradov SA, Boas DA (2010) Two-photon high-resolution 3D imaging of partial pressure of oxygen in cerebral vasculature and tissue. Nat Methods 7:755–759
83. Lecoq J, Parpaleix A, Roussakis E, Ducros M, Houssen YG, Vinogradov SA, Charpak S (2011) Simultaneous two-photon imaging of oxygen and blood flow in deep cerebral vessels. Nat Med 17:893–898
84. Devor A, Sakadzic S, Saisan PA, Yaseen MA, Roussakis E, Srinivasan VJ, Vinogradov SA, Rosen BR, Buxton RB, Dale AM, Boas DA (2011) "Overshoot" of O2 is required to maintain baseline tissue oxygenation at locations distal to blood vessels. J Neurosci 31: 13676–13681
85. Tootell RB, Silverman MS, De Valois RL, Jacobs GH (1983) Functional organization of the second cortical visual area in primates. Science 220:737–739
86. Weber B, Keller AL, Reichold J, Logothetis NK (2008) The microvascular system of the striate and extrastriate visual cortex of the macaque. Cereb Cortex 18:2318–2330
87. Keller AL, Schuz A, Logothetis NK, Weber B (2011) Vascularization of cytochrome oxidase-rich blobs in the primary visual cortex of squirrel and macaque monkeys. J Neurosci 31: 1246–1253
88. Fatt I (1976) Polarographic oxygen sensors. CRC Press, Cleveland
89. Thompson JK, Peterson MR, Freeman RD (2003) Single-neuron activity and tissue oxygenation in the cerebral cortex. Science 299: 1070–1072
90. Viswanathan A, Freeman RD (2007) Neurometabolic coupling in cerebral cortex reflects synaptic more than spiking activity. Nat Neurosci 10:1308–1312
91. Offenhauser N, Thomsen K, Caesar K, Lauritzen M (2005) Activity-induced tissue oxygenation changes in rat cerebellar cortex: interplay of postsynaptic activation and blood flow. J Physiol 565:279–294
92. Erecinska M, Silver IA (2001) Tissue oxygen tension and brain sensitivity to hypoxia. Respir Physiol 128:263–276
93. Masamoto K, Takizawa N, Kobayashi H, Oka K, Tanishita K (2003) Dual responses of tissue partial pressure of oxygen after functional stimulation in rat somatosensory cortex. Brain Res 979:104–113
94. Sharan M, Vovenko EP, Vadapalli A, Popel AS, Pittman RN (2008) Experimental and theoretical studies of oxygen gradients in rat

pial microvessels. J Cereb Blood Flow Metab 28:1597–1604

95. Vazquez AL, Fukuda M, Tasker ML, Masamoto K, Kim SG (2010) Changes in cerebral arterial, tissue and venous oxygenation with evoked neural stimulation: implications for hemoglobin-based functional neuroimaging. J Cereb Blood Flow Metab 30: 428–439
96. Vovenko E (1999) Distribution of oxygen tension on the surface of arterioles, capillaries and venules of brain cortex and in tissue in normoxia: an experimental study on rats. Pflugers Arch 437:617–623
97. Koch CJ (2002) Measurement of absolute oxygen levels in cells and tissues using oxygen sensors and 2-nitroimidazole EF5. Methods Enzymol 352:3–31
98. Swartz HM, Clarkson RB (1998) The measurement of oxygen in vivo using EPR techniques. Phys Med Biol 43:1957–1975
99. Ahmad R, Kuppusamy P (2010) Theory, instrumentation, and applications of electron paramagnetic resonance oximetry. Chem Rev 110:3212–3236
100. Wang LV (2009) Multiscale photoacoustic microscopy and computed tomography. Nat Photonics 3:503–509
101. Fu D, Matthews TE, Ye T, Piletic IR, Warren WS (2008) Label-free in vivo optical imaging of microvasculature and oxygenation level. J Biomed Opt 13:040503
102. Ashkenazi S, Huang SW, Horvath T, Koo YE, Kopelman R (2008) Photoacoustic probing of fluorophore excited state lifetime with application to oxygen sensing. J Biomed Opt 13:034023
103. Geissbuehler M, Spielmann T, Formey A, Marki I, Leutenegger M, Hinz B, Johnsson K, Van De Ville D, Lasser T (2010) Triplet imaging of oxygen consumption during the contraction of a single smooth muscle cell (A7r5). Biophys J 98:339–349
104. Spielmann T, Blom H, Geissbuehler M, Lasser T, Widengren J (2010) Transient state monitoring by total internal reflection fluorescence microscopy. J Phys Chem B 114: 4035–4046
105. Mik EG, van Leeuwen TG, Raat NJ, Ince C (2004) Quantitative determination of localized tissue oxygen concentration in vivo by two-photon excitation phosphorescence lifetime measurements. J Appl Physiol 97: 1962–1969
106. Brinas RP, Troxler T, Hochstrasser RM, Vinogradov SA (2005) Phosphorescent oxygen sensor with dendritic protection and two-photon absorbing antenna. J Am Chem Soc 127:11851–11862
107. Srinivasan VJ, Sakadzic S, Gorczynska I, Ruvinskaya L, Wu W, Fujimoto JG, Boas DA (2010) Quantitative cerebral blood flow with optical coherence tomography. Opt Express 18:2477–2494
108. Srinivasan VJ, Sakadzic S, Gorczynska I, Ruvinskaya S, Wu W, Fujimoto JG, Boas DA (2009) Depth-resolved microscopy of cortical hemodynamics with optical coherence tomography. Opt Lett 34:3086–3088
109. Deneux T, Faugeras O, Takerkart S, Masson G, Vanzetta I (2011) A new variational method for erythrocyte velocity estimation in wide-field imaging in-vivo. IEEE Trans Med Imaging 30:1527–1545
110. Turner DA, Foster KA, Galeffi F, Somjen GG (2007) Differences in O2 availability resolve the apparent discrepancies in metabolic intrinsic optical signals in vivo and in vitro. Trends Neurosci 30:390–398
111. Nemoto M, Nomura Y, Sato C, Tamura M, Houkin K, Koyanagi I, Abe H (1999) Analysis of optical signals evoked by peripheral nerve stimulation in rat somatosensory cortex: dynamic changes in hemoglobin concentration and oxygenation. J Cereb Blood Flow Metab 19:246–259
112. Narayan SM, Esfahani P, Blood AJ, Sikkens L, Toga AW (1995) Functional increases in cerebral blood volume over somatosensory cortex. J Cereb Blood Flow Metab 15: 754–765
113. Narayan SM, Santori EM, Blood AJ, Burton JS, Toga AW (1994) Imaging optical reflectance in rodent barrel and forelimb sensory cortex. Neuroimage 1:181–190
114. Grinvald A (1992) Optical imaging of architecture and function in the living brain sheds new light on cortical mechanisms underlying visual perception. Brain Topogr 5: 71–75
115. Huang D, Swanson EA, Lin CP, Schuman JS, Stinson WG, Chang W, Hee MR, Flotte T, Gregory K, Puliafito CA et al (1991) Optical coherence tomography. Science 254: 1178–1181
116. Wojtkowski M, Bajraszewski T, Targowski P, Kowalczyk A (2003) Real-time in vivo imaging by high-speed spectral optical coherence tomography. Opt Lett 28:1745–1747
117. Harbig K, Chance B, Kovach AG, Reivich M (1976) In vivo measurement of pyridine nucleotide fluorescence from cat brain cortex. J Appl Physiol 41:480–488
118. Lothman E, Lamanna J, Cordingley G, Rosenthal M, Somjen G (1975) Responses of

electrical potential, potassium levels, and oxidative metabolic activity of the cerebral neocortex of cats. Brain Res 88:15–36

119. Mayevsky A (1984) Brain NADH redox state monitored in vivo by fiber optic surface fluorometry. Brain Res 319:49–68
120. Baraghis E, Devor A, Fang Q, Srinivasan VJ, Yaseen MA, Wu W, Lesage F, Ayata C, Kasischke KA, Boas DA, Sakadzic S (2011) Two-photon microscopy of cortical NADH fluorescence intensity changes: correcting contamination from the hemodynamic response. J Biomed Opt 16:106003
121. Kramer RS, Pearlstein RD (1979) Cerebral cortical microfluorometry at isosbestic wavelengths for correction of vascular artifact. Science 205:693–696
122. Boas DA, Jones SR, Devor A, Huppert TJ, Dale AM (2008) A vascular anatomical network model of the spatio-temporal response to brain activation. Neuroimage 40:1116–1129
123. Devor A, Ulbert I, Dunn AK, Narayanan SN, Jones SR, Andermann ML, Boas DA, Dale AM (2005) Coupling of the cortical hemodynamic response to cortical and thalamic neuronal activity. Proc Natl Acad Sci USA 102: 3822–3827
124. Hillman EM (2007) Optical brain imaging in vivo: techniques and applications from animal to man. J Biomed Opt 12:051402
125. Berwick J, Johnston D, Jones M, Martindale J, Martin C, Kennerley AJ, Redgrave P, Mayhew JE (2008) Fine detail of neurovascular coupling revealed by spatiotemporal analysis of the hemodynamic response to single whisker stimulation in rat barrel cortex. J Neurophysiol 99:787–798
126. Devor A, Hillman EM, Tian P, Waeber C, Teng IC, Ruvinskaya L, Shalinsky MH, Zhu H, Haslinger RH, Narayanan SN, Ulbert I, Dunn AK, Lo EH, Rosen BR, Dale AM, Kleinfeld D, Boas DA (2008) Stimulus-induced changes in blood flow and 2-deoxyglucose uptake dissociate in ipsilateral somatosensory cortex. J Neurosci 28:14347–14357
127. Devor A, Tian P, Nishimura N, Teng IC, Hillman EM, Narayanan SN, Ulbert I, Boas DA, Kleinfeld D, Dale AM (2007) Suppressed neuronal activity and concurrent arteriolar vasoconstriction may explain negative blood oxygenation level-dependent signal. J Neurosci 27:4452–4459
128. Bouchard MB, Chen BR, Burgess SA, Hillman EM (2009) Ultra-fast multispectral optical imaging of cortical oxygenation, blood flow, and intracellular calcium dynamics. Opt Express 17:15670–15678
129. Calcinaghi N, Jolivet R, Wyss MT, Ametamey SM, Gasparini F, Buck A, Weber B (2011) Metabotropic glutamate receptor mGluR5 is not involved in the early hemodynamic response. J Cereb Blood Flow Metab 31: e1–e10
130. Jones PB, Shin HK, Boas DA, Hyman BT, Moskowitz MA, Ayata C, Dunn AK (2008) Simultaneous multispectral reflectance imaging and laser speckle flowmetry of cerebral blood flow and oxygen metabolism in focal cerebral ischemia. J Biomed Opt 13:044007
131. Polimeni JR, Granquist-Fraser D, Wood RJ, Schwartz EL (2005) Physical limits to spatial resolution of optical recording: clarifying the spatial structure of cortical hypercolumns. Proc Natl Acad Sci USA 102:4158–4163
132. Tian P, Teng IC, May LD, Kurz R, Lu K, Scadeng M, Hillman EM, De Crespigny AJ, D'Arceuil HE, Mandeville JB, Marota JJ, Rosen BR, Liu TT, Boas DA, Buxton RB, Dale AM, Devor A (2010) Cortical depth-specific microvascular dilation underlies laminar differences in blood oxygenation level-dependent functional MRI signal. Proc Natl Acad Sci USA 107:15246–15251
133. Boas D, Culver J, Stott J, Dunn A (2002) Three dimensional Monte Carlo code for photon migration through complex heterogeneous media including the adult human head. Opt Express 10:159–170
134. Tian P, Devor A, Sakadzic S, Dale AM, Boas DA (2010) Monte Carlo simulation of the spatial resolution and depth sensitivity of two-dimensional optical imaging of the brain. J Biomed Opt 16:016006
135. Wilson BC, Adam G (1983) A Monte Carlo model for the absorption and flux distributions of light in tissue. Med Phys 10:24–830
136. Chen BR, Bouchard MB, McCaslin AF, Burgess SA, Hillman EM (2011) High-speed vascular dynamics of the hemodynamic response. Neuroimage 54:1021–1030
137. Tian P, Teng IC, Dunn AK, Boas DA, Dale AM, Devor A (2007) Hemodynamic augmentation in response to a paired whisker stimulus as a function of cortical distance. In: Program No. 87.6. Neuroscience 2007 abstracts, Society for Neuroscience, San Diego. Online
138. Vinogradov SA, Lo LW, Jenkins WT, Evans SM, Koch C, Wilson DF (1996) Noninvasive imaging of the distribution in oxygen in tissue in vivo using near-infrared phosphors. Biophys J 70:1609–1617
139. Sakadzic S, Yuan S, Dilekoz E, Ruvinskaya S, Vinogradov SA, Ayata C, Boas DA (2009)

Simultaneous imaging of cerebral partial pressure of oxygen and blood flow during functional activation and cortical spreading depression. Appl Opt 48:D169–D177

140. Apreleva SV, Wilson DF, Vinogradov SA (2006) Tomographic imaging of oxygen by phosphorescence lifetime. Appl Opt 45:8547–8559
141. Golub AS, Barker MC, Pittman RN (2007) PO2 profiles near arterioles and tissue oxygen consumption in rat mesentery. Am J Physiol Heart Circ Physiol 293:H1097–H1106
142. Golub AS, Pittman RN (2008) PO2 measurements in the microcirculation using phosphorescence quenching microscopy at high magnification. Am J Physiol Heart Circ Physiol 294:H2905–H2916
143. Yaseen MA, Srinivasan VJ, Sakadzic S, Wu W, Ruvinskaya S, Vinogradov SA, Boas DA (2009) Optical monitoring of oxygen tension in cortical microvessels with confocal microscopy. Opt Express 17:22341–22350
144. Wilson DF, Vinogradov SA, Grosul P, Vaccarezza MN, Kuroki A, Bennett J (2005) Oxygen distribution and vascular injury in the mouse eye measured by phosphorescence-lifetime imaging. Appl Opt 44:5239–5248
145. Shonat RD, Kight AC (2003) Oxygen tension imaging in the mouse retina. Ann Biomed Eng 31:1084–1096
146. Shonat RD, Wilson DF, Riva CE, Pawlowski M (1992) Oxygen distribution in the retinal and choroidal vessels of the cat as measured by a new phosphorescence imaging method. Appl Opt 31:3711–3718
147. Ponticorvo A, Dunn AK (2010) Simultaneous imaging of oxygen tension and blood flow in animals using a digital micromirror device. Opt Express 18:8160–8170
148. Sinks LE, Robbins GP, Roussakis E, Troxler T, Hammer DA, Vinogradov SA (2010) Two-photon microscopy of oxygen: polymersomes as probe carrier vehicles. J Phys Chem B 114:14373–14382
149. Garaschuk O, Milos RI, Konnerth A (2006) Targeted bulk-loading of fluorescent indicators for two-photon brain imaging in vivo. Nat Protoc 1:380–386
150. Boorman L, Kennerley AJ, Johnston D, Jones M, Zheng Y, Redgrave P, Berwick J (2010) Negative blood oxygen level dependence in the rat: a model for investigating the role of suppression in neurovascular coupling. J Neurosci 30:4285–4294
151. Kennerley AJ, Berwick J, Martindale J, Johnston D, Papadakis N, Mayhew JE (2005) Concurrent fMRI and optical measures for the investigation of the hemodynamic response function. Magn Reson Med 54:354–365
152. Stosiek C, Garaschuk O, Holthoff K, Konnerth A (2003) In vivo two-photon calcium imaging of neuronal networks. Proc Natl Acad Sci USA 100:7319–7324